

## Dynamics of the Gas-Phase Reactions of Chloride Ion with Fluoromethane: High Excess Translational Activation Energy for an Endothermic S<sub>N</sub>2 Reaction

Laurence A. Angel, Sandra P. Garcia, and Kent M. Ervin\*

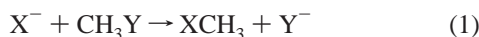
Contribution from the Department of Chemistry and Chemical Physics Program,  
University of Nevada, Reno, Nevada 89557

Received August 22, 2001

**Abstract:** Guided ion beam tandem mass spectrometry techniques are used to examine the competing product channels in the reaction of Cl<sup>-</sup> with CH<sub>3</sub>F in the center-of-mass collision energy range 0.05–27 eV. Four anionic reaction products are detected: F<sup>-</sup>, CH<sub>2</sub>Cl<sup>-</sup>, FCl<sup>-</sup>, and CHCl<sup>-</sup>. The endothermic S<sub>N</sub>2 reaction Cl<sup>-</sup> + CH<sub>3</sub>F → CH<sub>3</sub>Cl + F<sup>-</sup> has an energy threshold of E<sub>0</sub> = 181 ± 14 kJ/mol, exhibiting a 52 ± 16 kJ/mol effective barrier in excess of the reaction endothermicity. The potential energy of the S<sub>N</sub>2 transition state is well below the energy of the products. Dynamical impedances to the activation of the S<sub>N</sub>2 reaction are discussed, including angular momentum constraints, orientational effects, and the inefficiency of translational energy in promoting the reaction. The fluorine abstraction reaction to form CH<sub>3</sub> + FCl<sup>-</sup> exhibits a 146 ± 33 kJ/mol effective barrier above the reaction endothermicity. Direct proton transfer to form HCl is highly inefficient, but HF elimination is observed above 268 ± 95 kJ/mol. Potential energy surfaces for the reactions are calculated using the CCSD(T)/aug-cc-pVDZ and HF/6-31+G(d) methods and used to interpret the dynamics.

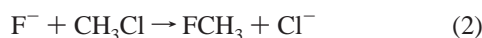
### Introduction

Experimental<sup>1</sup> and theoretical<sup>2,3</sup> studies of gas-phase bimolecular nucleophilic substitution (S<sub>N</sub>2) in halomethanes have provided detailed information on the dynamics, mechanisms, and energy dependence of reaction 1, where X and Y are halogen atoms.



The strong attraction between the halide ion and the dipolar halomethane results in a double-well potential energy surface.<sup>4–6</sup> The two potential energy minima correspond to the formation of ion–molecule intermediates on both the reactant and the product sides of the reaction. The two minima are separated by a central energy barrier corresponding to the five-coordinate [X–CH<sub>3</sub>–Y]<sup>-</sup> transition state.

We recently applied guided ion beam mass spectrometry techniques to investigate the cross section behavior of reaction 2 in the collision energy range 0.05–30 eV.<sup>7</sup> The exothermic



reaction 2 dominates at the lowest collision energies with two

independent endothermic reactions, proton transfer and halide abstraction, contributing at collision energies between 1 and 20 eV. Here we present complementary work on the reverse endothermic reaction 3. This investigation is one of the first



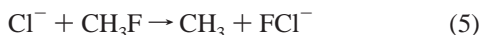
detailed energy-resolved studies of an endothermic S<sub>N</sub>2 reaction. The only other report of a strongly endothermic S<sub>N</sub>2 reaction, to our knowledge, is that of Zellermann and Vietzke,<sup>8</sup> who used an ion beam/gas cell technique without initial mass selection to measure the collision energy dependence of the products H<sup>-</sup>, F<sup>-</sup>, FBr<sup>-</sup>, and CH<sub>2</sub>Br<sup>-</sup> from the reaction Br<sup>-</sup> + CH<sub>3</sub>F, and the products F<sup>-</sup>, FI<sup>-</sup>, and CH<sub>2</sub>I<sup>-</sup> from the reaction I<sup>-</sup> + CH<sub>3</sub>F. The halogen abstraction reaction, resulting in the XY<sup>-</sup> ion, has also been observed in three previous guided ion beam experiments—the ClBr<sup>-</sup> ion from the reaction Cl<sup>-</sup> + CH<sub>3</sub>Br,<sup>9</sup> the Cl<sub>2</sub><sup>-</sup> ion from the reaction Cl<sup>-</sup> + CH<sub>3</sub>Cl,<sup>10</sup> and the FCl<sup>-</sup> ion in our previous work on reaction 2.<sup>7</sup>

Here we show that in the collision energy range 2–27 eV the endothermic reactions 4–6 can be driven by translational energy in competition with reaction 3.



\* Corresponding author. E-mail: ervin@chem.unr.edu.  
 (1) Chabinyk, M. L.; Craig, S. L.; Regan, C. K.; Brauman, J. I. *Science* **1998**, *279*, 1882–1886.  
 (2) Shaik, S. S.; Schlegel, H. B.; Wolfe, S. *Theoretical Aspects of Physical Organic Chemistry: The S<sub>N</sub>2 Mechanism*; John Wiley and Sons: New York, 1992.  
 (3) Hase, W. L. *Science* **1994**, *266*, 998–1002.  
 (4) Olmstead, W. N.; Brauman, J. I. *J. Am. Chem. Soc.* **1977**, *99*, 4219–4228.  
 (5) Dodd, J. A.; Brauman, J. I. *J. Phys. Chem.* **1986**, *90*, 3559–3562.  
 (6) Brauman, J. I. *J. Mass Spectrom.* **1995**, *30*, 1649–1650.  
 (7) Angel, L.; Ervin, K. *J. Phys. Chem. A* **2001**, *105*, 4042–4051.

(8) Zellermann, G.; Vietzke, E. *Radiochem. Acta* **1990**, *50*, 107–115.  
 (9) Cyr, D. A.; Scarton, M. G.; Wiberg, K. B.; Johnson, M. A.; Nonose, S.; Hirokawa, J.; Tanaka, H.; Kondow, T.; Morris, R. A.; Viggiano, A. A. *J. Am. Chem. Soc.* **1995**, *117*, 1828–1832.  
 (10) DeTuri, V. F.; Hintz, P. A.; Ervin, K. M. *J. Phys. Chem. A* **1997**, *101*, 5969–5986.



The possible mechanisms of reactions 3–6 can be broadly divided into the two categories of back-side and front-side attack. For the back-side attack, the path of the approaching  $\text{Cl}^-$  lies on the methyl side of  $\text{CH}_3\text{F}$ . The  $\text{S}_{\text{N}}2$  mechanism for reaction 1 proceeds through a back-side attack at carbon, resulting in inversion of the methyl group. In the front-side attack mechanism, the  $\text{Cl}^-$  approaches the  $\text{CH}_3\text{F}$  molecule from the C–F bond side and may lead to displacement or abstraction. To help investigate the microscopic reaction mechanisms for reactions 3–6, the coupled cluster CCSD(T)/aug-cc-pVDZ and HF/6-31+G(d) methods are used to calculate potential energy surfaces (PES).

### Experimental Methods

Chloride anions are produced in a microwave discharge source from tetrachloromethane,  $\text{CCl}_4$ , added in trace amounts in a flowing buffer gas of helium. The  $\text{Cl}^-$  anions pass along a flow tube and are sampled through a nose cone into the guided ion beam tandem mass spectrometer.<sup>10</sup> The anions are then shaped, focused, and accelerated by a series of lenses to a magnetic mass spectrometer, which mass selects the  $^{35}\text{Cl}^-$  ions before they are injected into an octopole radio frequency ion trap. Situated at the center of the octopole is a reaction cell where the fluoromethane (Matheson Tri-Gas, 99%) reactant gas is introduced. The collision energy between the chloride ions and the neutral fluoromethane is controlled by the dc potential difference between the flow tube ion source and the octopole. The anionic reactants and products are then extracted from the octopole and injected into a quadrupole mass spectrometer where they are mass analyzed. Ion intensities are detected by a collision dynode/channeltron multiplier operated in negative-ion pulse counting mode.

Absolute reaction cross sections are determined as a function of collision energy by scanning the octopole dc potential and counting the reactant and product ions for predetermined dwell times.<sup>10</sup> The laboratory ion energy is measured using retarding potential analysis, confirmed by time-of-flight measurements, and converted to relative collision energy,  $E$ , in the center-of-mass (c.m.) frame.<sup>10,11</sup> Background ion counts occurring outside the reaction cell are also collected and subtracted from the total. All cross sections are measured at three pressures in the range  $(5\text{--}20) \times 10^{-5}$  mbar. The results are extrapolated to zero pressure by a least-squares linear regression, ensuring that the reported cross sections are in the single-collision limit.<sup>10,11</sup>

The threshold behavior of the cross section,  $\sigma(E)$ , is modeled by using an empirical threshold law,<sup>10–14</sup>

$$\sigma(E) = \sigma_0 \sum_i g_i [E + E_i - E_0]^N / E \quad (7)$$

where  $E_i$  is the internal energy of reactant state  $i$  with fractional thermal population  $g_i$  corresponding to a Boltzmann distribution at 300 K,  $\sigma_0$  and  $N$  are adjustable parameters, and  $E_0$  is the 0 K reaction threshold energy. Experimental<sup>15</sup> vibrational frequencies and rotational constants of  $\text{CH}_3\text{F}$  are used for the sum over the reactant internal energy density of states.<sup>13,14</sup> Finally, eq 7 is convoluted over the experimental collision energy distributions<sup>16,17</sup> as described previously.<sup>11</sup> These calculations are performed using the CRUNCH data analysis program.<sup>18</sup>

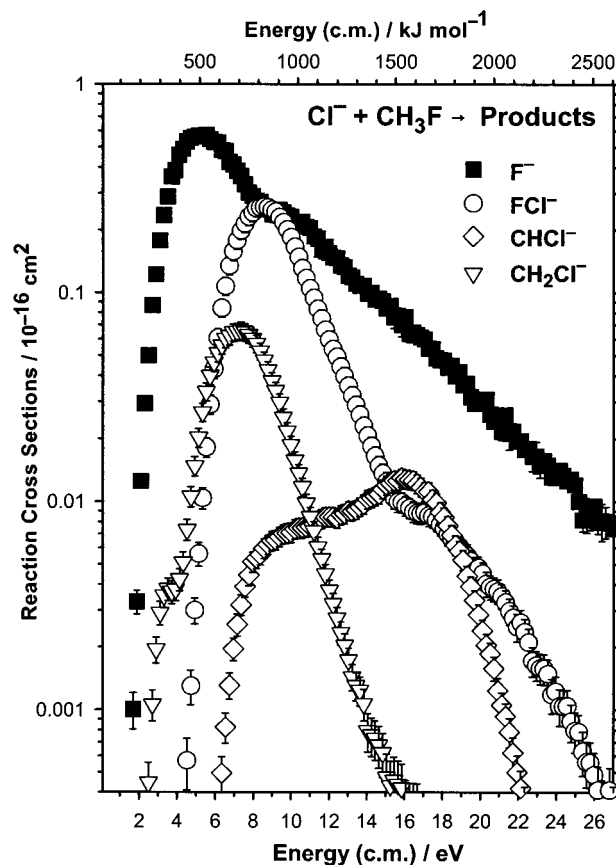


**Figure 1.** Cross sections for the product ions  $\text{F}^-$ ,  $\text{CH}_2\text{Cl}^-$ ,  $\text{FCl}^-$ , and  $\text{CHCl}^-$  from the reaction of  $\text{Cl}^- + \text{CH}_3\text{F}$  as a function of relative collision energy in the center-of-mass frame.

The reported error limits are propagated from individual sources of uncertainty (assuming they are independent of each other) and represent  $\pm 2$  combined standard uncertainties<sup>19</sup> or an approximate 95% confidence level. Uncertainties are included for the determination of the ion beam energy zero, the reproducibility of data taken on separate occasions, the vibrational frequencies, the least-squares fit of eq 7, and the consistency of the fits using different energy ranges.

### Results

The experimental reaction cross sections from 0.05 to 27 eV c.m. are shown in Figure 1. Four product ions,  $\text{F}^-$ ,  $\text{CH}_2\text{Cl}^-$ ,  $\text{FCl}^-$ , and  $\text{CHCl}^-$ , are observed from reactions 3–6. Table 1 lists experimental endothermicities of possible product channels.<sup>20–29</sup> The mass ranges of the octopole and quadrupole prevent detection of light products,  $\text{H}^-$  or  $\text{e}^-$ . In survey mass spectra, a few ion counts per second of  $\text{CH}_2\text{F}^-$  were sometimes observed, but the signal was near the detection limit of the GIB apparatus and the channel was too weak to obtain cross sections as a function of energy. The  $\text{S}_{\text{N}}2$  product ion  $\text{F}^-$  from reaction 3 is detected at the lowest collision energies. The cross section rises from approximately 1.5 eV and exhibits a maximum of

(15) Herzberg, G. *Molecular Spectra and Molecular Structure II. Infrared and Raman Spectra of Polyatomic Molecules*; Van Nostrand Reinhold: New York, 1945.

(16) Chantry, P. J. *J. Chem. Phys.* **1971**, *55*, 2746–2759.

(17) Lifshitz, C.; Wu, R.; Tieman, T. O.; Terwilliger, D. T. *J. Chem. Phys.* **1978**, *68*, 247–260.

(18) Armentrout, P. B.; Ervin, K. M. *CRUNCH*; Fortran program.

(19) Taylor, B. N.; Kuyatt, C. *Guidelines for Evaluating and Expressing the Uncertainty of NIST Measurement Results*; NIST Technical Note 1297; National Institute of Standards and Technology: Washington, DC, 1994 (<http://physics.nist.gov/Document/tl1297.pdf>).

(11) Ervin, K. M.; Armentrout, P. B. *J. Chem. Phys.* **1985**, *83*, 166–189.

(12) Armentrout, P. B. *Int. J. Mass Spectrom.* **2000**, *200*, 219–241.

(13) Schultz, R. H.; Crellin, K. C.; Armentrout, P. B. *J. Am. Chem. Soc.* **1991**, *113*, 8590–8601.

(14) Dalleska, N. F.; Honma, K.; Sunderlin, L. S.; Armentrout, P. B. *J. Am. Chem. Soc.* **1994**, *116*, 3519–3528.

**Table 1.** Threshold Energies and Enthalpies for the Reaction  $\text{Cl}^- + \text{CH}_3\text{F} \rightarrow \text{Products}$  ( $\text{kJ mol}^{-1}$ )

reaction	products	$E_0$ (this work)	$N^b$	$\Delta H_0$ (exptl) <sup>b</sup>	$\Delta H_0$ (G3) <sup>c</sup>	$\Delta H_0$ (CCSD(T)/aug-cc-pVDZ) <sup>d</sup>
	$\text{Cl}^- + \text{CH}_3\text{F}$	0		0	0	0
3	$\text{F}^- + \text{CH}_3\text{Cl}$	$181 \pm 14$	2.5	$129 \pm 8^e$	134	133
4	$\text{CH}_2\text{Cl}^- + \text{HF}$	$268 \pm 95$	1.0	$223 \pm 20^f$	237	238
	$\text{CH}_2\text{Cl} + \text{HF} + \text{e}^-$			$300 \pm 13$	304	
	$\text{CH}_2\text{F}^- + \text{HCl}$			$309 \pm 21^g$	320	
5	$\text{FCl}^- + \text{CH}_3$	$465 \pm 24$	2.5	$319 \pm 22^h$	325	314
	$\text{CH}_2\text{F} + \text{HCl} + \text{e}^-$			$333 \pm 13$	338	
	$\text{H}^- + \text{CH}_2\text{ClF}$			$334 \pm 22$	370	
	$\text{Cl}^- + \text{CH}_2 + \text{HF}$			$341 \pm 9$	342	
	$\text{Cl} + \text{CH}_3\text{F} + \text{e}^-$			$348 \pm 11$	348	
	$\text{H} + \text{CH}_2\text{ClF} + \text{e}^-$			$407 \pm 22$	417	
	$\text{Cl}^- + \text{CH}_2\text{F} + \text{H}$			$434 \pm 18$	417	
	$\text{Cl}^- + \text{F} + \text{CH}_3$			$452 \pm 8$	452	
	$\text{F} + \text{CH}_3\text{Cl} + \text{e}^-$			$457 \pm 8$	462	
8	$\text{F}^- + \text{Cl} + \text{CH}_3$			$472 \pm 8$	472	
	$\text{FCl} + \text{CH}_3 + \text{e}^-$			$547 \pm 8$	551	
6	$\text{CHCl}^- + \text{HF} + \text{H}$	$653 \pm 26$	0.5	$588 \pm 31^i$	604	585
	$\text{Cl} + \text{CH}_2 + \text{HF} + \text{e}^-$			$690 \pm 9$	690	
9	$\text{CHCl}^- + \text{H}_2 + \text{F}$			$722 \pm 31^i$	737	
	$\text{Cl} + \text{CH}_2\text{F} + \text{H} + \text{e}^-$			$761 \pm 13$	766	
	$\text{FCl}^- + \text{CH} + \text{H}_2$			$763 \pm 22^h$	766	
	$\text{FCl}^- + \text{CH}_2 + \text{H}$			$775 \pm 22^h$	783	
	$\text{Cl} + \text{F} + \text{CH}_3 + \text{e}^-$			$800 \pm 8$	800	
	$\text{CH}_2\text{Cl}^- + \text{H} + \text{F}$			$790 \pm 20^g$	804	

<sup>a</sup> Fitting parameter in eq 7. <sup>b</sup> Enthalpies of reactions calculated with enthalpies of formation values cited in Gurvich et al.<sup>20,21</sup> except as noted. <sup>c</sup> Calculated here or obtained from <http://chemistry.anl.gov/compmat/comptherm.htm>.<sup>22</sup> <sup>d</sup> Corrected for zero-point energy from frequencies calculated at the B3LYP/aug-cc-pVDZ level. <sup>e</sup> From  $\Delta_f H_0(\text{CH}_3\text{F}) = -225 \pm 8$  kJ/mol estimated by Kolesov,<sup>23</sup> which agrees with theoretical calculations by Berry et al.<sup>24</sup> <sup>f</sup> Calculated using  $\text{EA}(\text{CH}_2\text{Cl}) = 0.80 \pm 0.16$  eV determined by Bartmess from work by Ingemann and Nibbering.<sup>25</sup> <sup>g</sup> Calculated using  $\Delta_f H_0(\text{CH}_2\text{F}^-) = -53 \pm 19$  kJ/mol determined by Bartmess<sup>26</sup> from work by Graul and Squires.<sup>27</sup> <sup>h</sup> Calculated using  $\text{EA}(\text{FCl}) = 2.37 \pm 0.21$  eV published by Dudin et al.<sup>28</sup> <sup>i</sup> Calculated using  $\text{EA}(\text{CHCl}) = 1.210 \pm 0.005$  eV published by Gilles et al.<sup>29</sup>

$0.6 \times 10^{-16}$  cm<sup>2</sup> at about 5 eV, before declining at energies above 6 eV. The cross section for methylene abstraction, reaction 4, exhibits a dual rising feature. An initial small rise at 2.5 eV to  $0.004 \times 10^{-16}$  cm<sup>2</sup> is followed by a second onset originating at about 4 eV. The second feature rises to a maximum of  $0.07 \times 10^{-16}$  cm<sup>2</sup> at about 8 eV before declining to the experimental detection limit by 16 eV. The  $\text{FCl}^-$  ion is the product of halide abstraction reaction 5 and exhibits a rising cross section from about 4.5 eV. At 9 eV, the  $\text{FCl}^-$  cross section exhibits a maximum of  $0.3 \times 10^{-16}$  cm<sup>2</sup>. As the  $\text{FCl}^-$  cross section starts to decline at energies above 9 eV, there is a small but observable increase in the  $\text{F}^-$  cross section, evidence that there is a small contribution from reaction 8 to  $\text{F}^-$  formation. Finally, originating



at apparent collision energies of 6 eV, the  $\text{CHCl}^-$  ion from

reaction 6 is detected. After an initial steep rise, the  $\text{CHCl}^-$  cross section continues to rise more slowly and forms a peak at about 17 eV, suggesting that reaction 9, a more endothermic process (Table 1), is also contributing at these higher energies.



Threshold energies,  $E_0$ , for the four endothermic reactions 3–6 are obtained by fits to eq 7 and are compared with established thermochemical values in Table 1. The fits of the empirical threshold law to the rising experimental cross section data are shown in Figure 2. Reactions 3, 5, and 6 all exhibit steep cross-section rises, allowing for reasonable empirical threshold fits. For reactions 3 and 5, good fits using eq 7 can be achieved up to only about 2 eV above the apparent threshold. Reaction 4 exhibits a small initial rise in the cross section, resulting in a large uncertainty in the threshold energy.

### Theoretical Methods and Potential Energy Surfaces

Coupled cluster (CCSD(T)),<sup>30</sup> density functional theory (B3LYP),<sup>31</sup> Hartree–Fock (HF), and Gaussian-3 (G3)<sup>22</sup> calculations have been performed using Gaussian 98.<sup>32</sup> The potential energy surfaces (PES)

- (20) Gurvich, L. V.; Veyts, I. V.; Alcock, C. B. *Thermodynamic Properties of Individual Substances*, 4th ed.; Hemisphere Publishing Corp.: New York, 1989; Vol. 1 (Elements O, H (D, T), F, Cl, Br, I, He, Ne, Ar, Kr, Xe, Rn, S, N, P and Their Compounds), Parts 1–2.
- (21) Gurvich, L. V.; Veyts, I. V.; Alcock, C. B. *Thermodynamic Properties of Individual Substances*, 4th ed.; Hemisphere: New York, 1991; Vol. 2 (Elements C, Si, Ge, Sn, Pb, and Their Compounds), Parts 1–2.
- (22) Curtiss, L. A.; Raghavachari, K.; Redfern, P. C.; Rassolov, V.; Pople, J. A. *J. Chem. Phys.* **1998**, *109*, 7764–7776. (Supplementary material at <http://chemistry.anl.gov/compmat/comptherm.htm>).
- (23) Kolesov, V. *Russ. Chem. Rev.* **1978**, *47*, 1145–1168.
- (24) Berry, R.; Burgess, D.; Nyden, M.; Zachariah, M.; Schwartz, M. *J. Phys. Chem.* **1995**, *99*, 17145–17150.
- (25) Ingemann, S.; Nibbering, N. M. M. *J. Chem. Soc., Perkin Trans. 2* **1985**, 837–840.
- (26) Bartmess, J. E. Negative Ion Energetics Data. In *NIST Chemistry WebBook, NIST Standard Reference Database Number 69*; Mallard, W. G.; Linstrom, P. J., Eds.; National Institute of Standards and Technology: Gaithersburg, MD, Feb 2000 (<http://webbook.nist.gov>).
- (27) Graul, S. T.; Squires, R. R. *J. Am. Chem. Soc.* **1990**, *112*, 2517–2529.
- (28) Dudin, A. V.; Gorokhov, L. N.; Baluev, A. V. *Izv. Akad. Nauk SSR Ser. Khim.* **1979**, 2408.
- (29) Gilles, M.; Ervin, K.; Ho, J.; Lineberger, W. *J. Phys. Chem.* **1992**, *96*, 1130–1141.

- (30) Pople, J. A.; Head-Gordon, M.; Raghavachari, K. *J. Chem. Phys.* **1987**, *87*, 5968–5975.
- (31) Becke, A. D. *J. Chem. Phys.* **1993**, *98*, 5648–5652.
- (32) Frisch, M. J.; Trucks, G. W.; Schlegel, H. B.; Scuseria, G. E.; Robb, M. A.; Cheeseman, J. R.; Zakrzewski, V. G.; Montgomery, J. A., Jr.; Stratmann, R. E.; Burant, J. C.; Dapprich, S.; Millam, J. M.; Daniels, A. D.; Kudin, K. N.; Strain, M. C.; Farkas, O.; Tomasi, J.; Barone, V.; Cossi, M.; Cammi, R.; Mennucci, B.; Pomelli, C.; Adamo, C.; Clifford, S.; Ochterski, J.; Petersson, G. A.; Ayala, P. Y.; Cui, Q.; Morokuma, K.; Malick, D. K.; Rabuck, A. D.; Raghavachari, K.; Foresman, J. B.; Cioslowski, J.; Ortiz, J. V.; Stefanov, B. B.; Liu, G.; Liashenko, A.; Piskorz, P.; Komaromi, I.; Gomperts, R.; Martin, R. L.; Fox, D. J.; Keith, T.; Al-Laham, M. A.; Peng, C. Y.; Nanayakkara, A.; Gonzalez, C.; Challacombe, M.; Gill, P. M. W.; Johnson, B. G.; Chen, W.; Wong, M. W.; Andres, J. L.; Head-Gordon, M.; Replogle, E. S.; Pople, J. A. *Gaussian 98*, revision A.6; Gaussian, Inc.: Pittsburgh, PA, 1998.

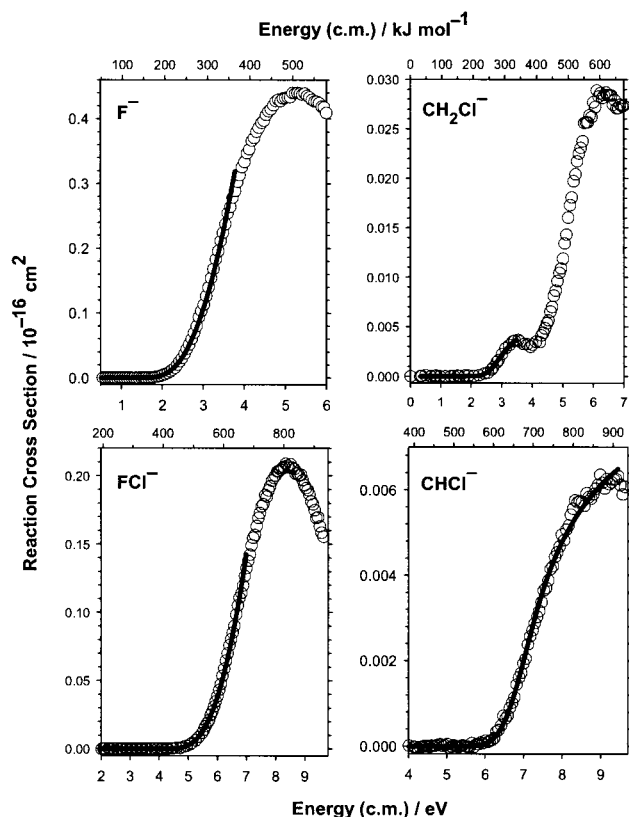


**Figure 2.** Cross sections for the threshold regions for reactions 3–6 as a function of relative collision energy in the center-of-mass frame. The circles are experimental data, and the solid lines are the best fits of eq 7 convoluted as described in the text.

for reactions 3 and 5 are calculated at the CCSD(T) level with the aug-cc-pVDZ basis set<sup>33</sup> and are shown in Figures 3–5. To avoid the high computational cost of CCSD(T) frequencies, the stationary points are confirmed by auxiliary geometry and frequency calculations at the B3LYP/aug-cc-pVDZ level,<sup>31</sup> which is also used for vibrational zero-point energy (ZPE) corrections. The CCSD(T)/aug-cc-pVDZ reaction enthalpies and calculated  $S_N2$  stationary point energies for reactions 3–6 are shown in Tables 1 and 2, respectively. Comparison of the CCSD(T)/aug-cc-pVDZ reaction enthalpies with the experimental thermochemical values show good correlation for reactions 3–6. G3 reaction enthalpies of a range of possible reactions resulting from  $\text{Cl}^- + \text{CH}_3\text{F}$  are also included in Table 1. The G3 reaction enthalpies show overall good agreement with the experimental reaction enthalpies.

## Results

The PES for reaction 3 has been calculated at the CCSD(T)/aug-cc-pVDZ level in  $C_{3v}$  symmetry and is shown in Figure 3, which includes the geometries of the entrance ion–dipole complex (**3a**), the  $S_N2$  transition-state central barrier (**3b**), and the ion–dipole exit complex (**3c**). The  $C_{3v}$  PES exhibits a central barrier height of 113.2 kJ/mol relative to **3a** and a small well for the exit  $C_{3v}$   $\text{F}^- \cdots \text{CH}_3\text{Cl}$  ion–dipole complex (**3c**) of 8 kJ/mol relative to **3b**, with corrections for ZPE as shown in Table 2. Previous studies using HF, MP2, B3LYP, QCISD, CCSD(T), and G2(+) have shown a wide variation of results for the depth of the  $C_{3v}$  **3c** well, with values of 0–26 kJ/mol.<sup>7,34–39</sup>

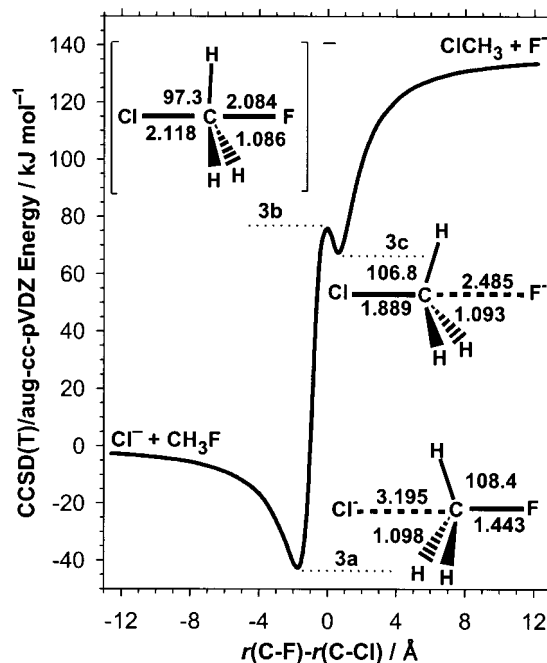


**Figure 3.** Potential energy surface for reaction 3 in  $C_{3v}$  symmetry. The energy relative to reactants calculated at the CCSD(T)/aug-cc-pVDZ level without ZPE correction is plotted versus the difference between the C–Cl and C–F bond lengths.

The authors<sup>37</sup> of the calculations at the highest level of theory, CCSD(T)/aug-cc-pVQZ, recommend  $13.8 \pm 1.3$  kJ/mol after considering basis set superposition error and additional electron correlation and basis set effects but without correction for ZPE.

Our previous work<sup>7</sup> on reaction 2 found that a restricted  $C_{3v}$  ion–dipole potential energy surface may be insufficient for describing the  $S_N2$  reaction because of the strong hydrogen-bonding propensity of the fluoride ion. The  $C_s$   $\text{F}^- \cdots \text{H}-\text{CH}_2\text{Cl}$  hydrogen-bonded complex is 5 kJ/mol more stable than the  $C_{3v}$   $\text{F}^- \cdots \text{CH}_3\text{Cl}$  ion–dipole complex at the CCSD(T)/aug-cc-pVDZ level (Table 2). Figure 4 shows the PES of reaction 3 recalculated in  $C_s$  symmetry and including the hydrogen-bonded  $\text{F}^- \cdots \text{H}-\text{CH}_2\text{Cl}$  complex **4b**. The depth of the exit well is now increased from 8 kJ/mol for **3c** to 13.2 kJ/mol for **4b** (Table 2). The PES exhibits a second transition state, **4a**, separating the two ion–molecule minima **3c** and **4b**. Figure 4 is constructed from CCSD(T)/aug-cc-pVDZ energy minimizations at all stationary points and along the curves with fixed  $r(\text{C}-\text{F})$  or  $r(\text{C}-\text{Cl})$ , except for the points that join the two minima to the transition state **4a**. These points are interpolated from a Synchronous Transit-Guided Quasi-Newton (QST3)<sup>40,41</sup> calculation of the reaction path at the B3LYP/aug-cc-pVDZ level, which confirms that the two minima (**3c** and **4b**) are connected by the transition state **4a**. (QST3 calculations at the CCSD(T) level were not feasible computationally.) Starting at the transition state **3b**, we can see that as the fluoride ion starts to exit along the  $C_{3v}$  axis, the PES shows an initial relaxation into the  $C_{3v}$  ion–dipole minimum **3c**. The ion–dipole minimum **3c**, however, is not the lowest energy ion–molecule intermediate in  $C_s$

(37) Botschwina, P.; Horn, M.; Seeger, S.; Oswald, R. *Ber. Bunsen-Ges. Phys. Chem.* **1997**, *101*, 387–390.

(38) Wang, H.; Hase, W. L. *J. Am. Chem. Soc.* **1997**, *119*, 3093–3102.

(39) Su, T.; Wang, H.; Hase, W. L. *J. Phys. Chem. A* **1998**, *102*, 9819–9828.

(40) Peng, C.; Schlegel, H. B. *Isr. J. Chem.* **1994**, *33*, 449.

(41) Peng, C.; Ayala, P. Y.; Schlegel, H. B.; Frisch, M. J. *J. Comput. Chem.* **1996**, *17*, 49–56.

(33) Woon, D. E.; Dunning, T. H., Jr. *J. Chem. Phys.* **1993**, *98*, 1358–1371.

(34) Wolfe, S. *Can. J. Chem.* **1984**, *62*, 1465.

(35) Shi, Z.; Boyd, R. J. *J. Am. Chem. Soc.* **1990**, *112*, 6789–6796.

(36) Glukhovtsev, M. N.; Pross, A.; Radom, L. *J. Am. Chem. Soc.* **1996**, *118*, 6273–6284.

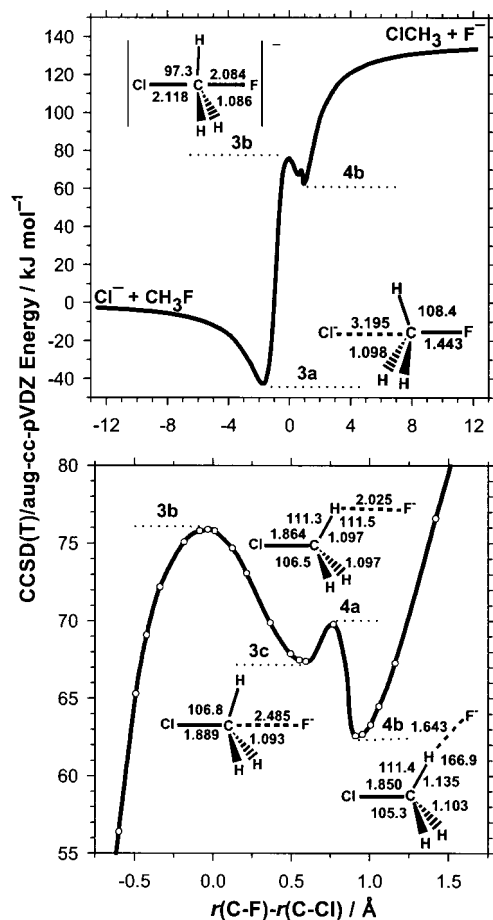


**Figure 4.** Potential energy surface for reaction 3 in  $C_s$  symmetry. The energy relative to reactants calculated at the CCSD(T)/aug-cc-pVDZ level without ZPE correction is plotted versus the difference between the C–Cl and C–F bond lengths and includes the  $C_s$  hydrogen-bonded minimum energy complex. The lower plot is a detail of the area on the  $C_s$  potential energy surface, where the two ion–molecule minima are separated by a  $C_s$  transition state.

symmetry, and the complex may further relax to the hydrogen-bonded complex **4b** if it first passes over the  $C_s$  transition state structure **4a**, which is 1.8 kJ/mol higher in energy than **3c** (Table 2). The energy needed to pass over the lower transition state corresponds to approximately one quantum of Cl–C–F bend vibrational energy (1.6 kJ/mol). The three-fold degenerate complex **4b** on the PES effectively deepens the well of the exit ion–molecule intermediate and in turn may influence the reactivity and final products of the  $\text{Cl}^- + \text{CH}_3\text{F}$  reaction, as will be discussed in more detail below.

The PES for the halophilic attack reaction (eq 5) in  $C_{3v}$  symmetry is shown in Figure 5. The PES exhibits a repulsive entrance surface with a steep exit channel out to the products  $\text{FCl}^-$  and  $\text{CH}_3$ . There is no minimum potential energy structure along the repulsive surface. To model the exit channel out to the correct products, the PES in that region is calculated using the unrestricted method UCCSD(T)/aug-cc-pVDZ. This is necessary because the restricted CCSD(T)/aug-cc-pVDZ method dissociates into  $\text{FCl}^{2-}$  and  $\text{CH}_3^+$ . The unrestricted wave function exhibits a considerable amount of spin contamination, so the overall results may have only qualitative significance. However, the calculation implies that there is no significant intrinsic barrier in excess of the endoergicity for reaction 5. A small feature in the exit surface of the PES at  $r(\text{C–F})-r(\text{Cl–F})$  distances

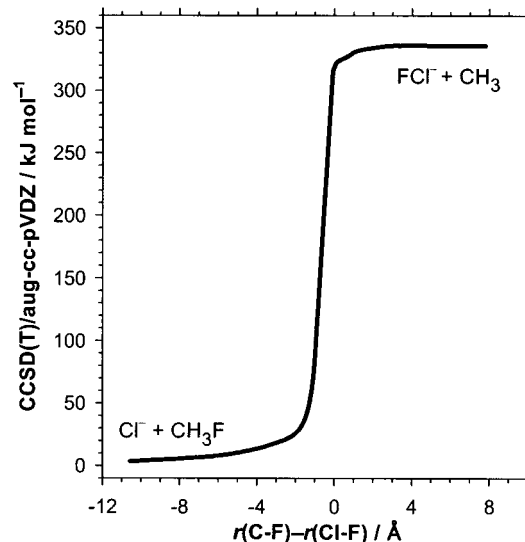


**Figure 5.** Potential energy surface for reaction 5 with  $C_s$  symmetry. The energy relative to reactants calculated at the CCSD(T)/aug-cc-pVDZ level without ZPE correction is plotted versus the difference between the C–Cl and Cl–F bond lengths.

**Table 2.** Stationary State Energies ( $\text{kJ mol}^{-1}$ )

complex or transition state	CCSD(T)/ aug-cc-pVDZ <sup>a</sup>	CCSD(T)/ aug-cc-pVQZ <sup>b</sup>
<b>3a</b> $C_{3v}$ $\text{Cl}^- \cdots \text{CH}_3\text{F}$ ion–dipole complex	−41.7	−39.3 (−40.2)
<b>3b</b> $C_{3v}$ $[\text{Cl}-\text{CH}_3-\text{F}]^-$ transition state	71.5	80.0 (84.4)
<b>3c</b> $C_{3v}$ $\text{CH}_3\text{C} \cdots \text{F}^-$ ion–dipole complex	63.5	67.7 (71.6)
<b>4a</b> $C_s$ $[\text{Cl}-\text{CH}_3-\text{F}]^-$ transition state	65.3	
<b>4b</b> $C_s$ $\text{ClCH}_2-\text{H} \cdots \text{F}^-$ hydrogen-bonded complex	58.3	

<sup>a</sup> Energies at 0 K relative to  $\text{Cl}^- + \text{CH}_3\text{F}$  reactants and corrected for zero-point energy calculated at the B3LYP/aug-cc-pVDZ level. <sup>b</sup> Botschwina et al.<sup>37</sup> Values include B3LYP/aug-cc-pVDZ zero-point energies with the original reported values reported in parentheses.

between 0 and 1 Å is the result of partial inversion of  $\text{CH}_3$  due to the attraction of the departing  $\text{FCl}^-$ , followed by reversion to the asymptotic planar geometry.

We have used HF/6-31+G(d) calculations to illustrate the topology of the PES for reactions 2 and 3 in two dimensions. The pseudo-collinear PES in  $C_{3v}$  symmetry is shown in Figure 6. The contour plot is mapped on a mass-weighted coordinate system<sup>42</sup> with the axes skewed at an angle of 51.4°. The positions of the hydrogen atoms are optimized for each pair of  $r(\text{C–Cl})$  and  $r(\text{C–F})$  values. Figure 6 shows that the energy barrier corresponding to **3b** lies nearer to  $\text{F}^- + \text{CH}_3\text{Cl}$  than to  $\text{Cl}^- + \text{CH}_3\text{F}$ . The stationary point geometries and relative energies at the HF/6-31+G(d) level are in qualitative agreement with the CCSD(T)/aug-cc-pVDZ calculations. The main difference is that the distances between the ion and the molecular species in **3a** and **3c** are 0.2 and 0.1 Å longer at the HF/6-31+G(d) level, respectively.

## Discussion

**$S_N2$  Reaction Cross Section Behavior.** The threshold energy from the fit of eq 7 to the cross section for reaction 3 shown in Figure 2 is  $E_0 = 181 \pm 14$  kJ/mol, or  $52 \pm 16$  kJ/mol in excess of the established experimental endothermicity (Table 1). Thus, the system exhibits a large excess barrier for translational

(42) Levine, R. D.; Bernstein, R. B. *Molecular Reaction Dynamics and Chemical Reactivity*; Oxford University Press: New York, 1987.

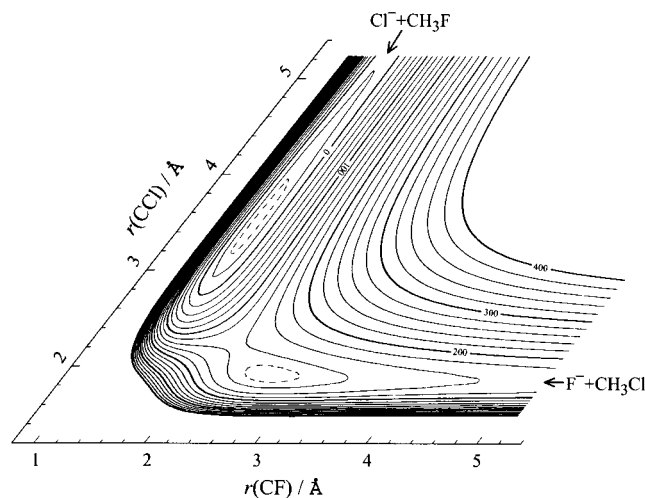


**Figure 6.** Contour plot of the potential energy surface of reaction 3 treated as a pseudo-collinear  $C_{3v}$  reaction. The contours are mapped on the mass-skewed coordinate system (see text). The potential energies are calculated at the HF/6-31+g(d) level. The contour intervals are 20 kJ/mol, with supplementary contours (dashed lines) at 130 and  $-30$  kJ/mol relative to  $\text{Cl}^- + \text{CH}_3\text{F}$ .

activation. The observed threshold energy does not necessarily represent an energy where the  $\text{S}_{\text{N}}2$  reaction suddenly turns on, but rather reflects the inefficiency of translational activation and the sensitivity threshold of the experiment (about  $0.0005 \text{ \AA}^2$ ). We previously calculated the energy of the  $C_s$  transition state ( $\text{CH}_3\text{ClF}^-$ ) for a front-side nucleophilic exchange mechanism.<sup>7</sup> The potential energy barrier for that process is about 99 kJ/mol above the products of reaction 3, which is too high to explain the observed reaction at its onset. Therefore, the system must pass over the  $\text{S}_{\text{N}}2$  central barrier, albeit at elevated energies.

The  $\text{S}_{\text{N}}2$  potential energy surface for reaction 3 (Figures 3 and 4) exhibits no energy barrier above the product energy. The excess translational activation energy for reaction 3, therefore, results from some constrictions that are not due to an overall energy barrier. This contrasts with the general behavior for endothermic ion–molecule reactions, which often yield threshold energies equal to the thermochemical endoergicity of reaction.<sup>12</sup> Among the known exceptions are cases with an actual potential energy barrier above the products, a change of spin or electronic state symmetry between reactants and products, or competition with a lower-energy channel, none of which applies here. For exothermic  $\text{S}_{\text{N}}2$  reactions, the double-well potential is known to cause inefficient reactivity even when the central barrier at the  $\text{S}_{\text{N}}2$  transition state lies well below the product energies. For instance, reaction 2, the reverse of reaction 3 in the exothermic direction, has a somewhat low reaction efficiency (56–61%) compared with the collision rate at thermal energies,<sup>7,43</sup> but it certainly does not show an activation energy approaching the  $52 \pm 16$  kJ/mol excess barrier that we observe for reaction 3. This behavior shows that the effective excess barrier for reaction 3 is dynamic in origin. Apparently, the influence of the  $\text{S}_{\text{N}}2$  central barrier is greatly magnified for the endothermic reaction. Here we discuss three effects that may contribute to the observed high threshold energy: angular momentum barriers, orientational or steric constraints, and translational versus vibrational energy requirements.

(43) Su, T.; Morris, R. A.; Viggiano, A. A.; Paulson, J. F. *J. Phys. Chem.* **1990**, *94*, 8426–8430.

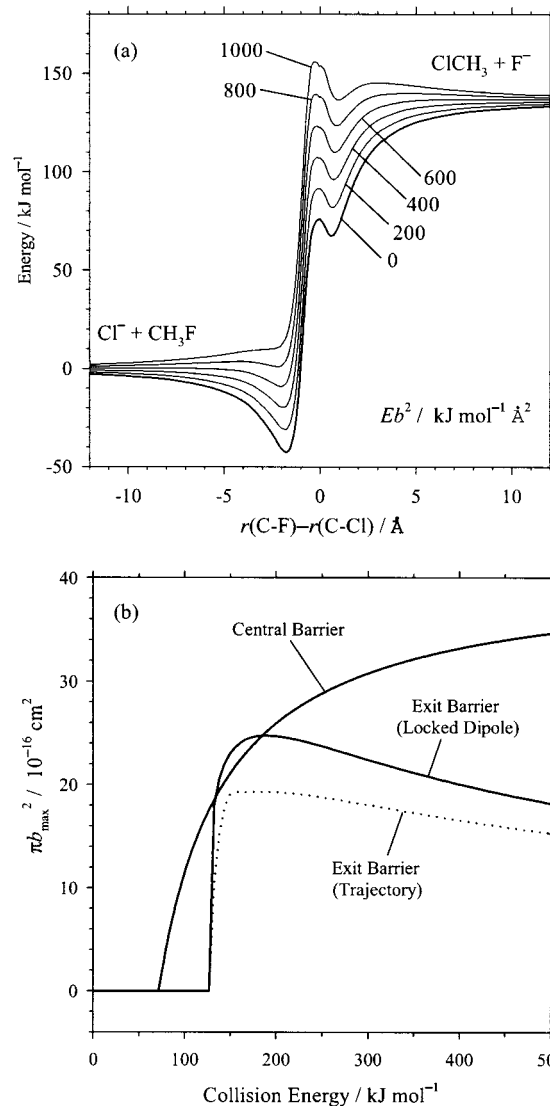


**Figure 7.** (a) Effective potential energy for reaction 3 in  $C_{3v}$  symmetry including the centrifugal potential energy term for various values of  $Eb^2$  as labeled in units of kilojoules per mole per square angstrom, where  $E$  is the relative collision energy and  $b$  is the impact parameter. (b) Collision theory cross sections for reaction 3 for crossing the central barrier and the exit barrier. The solid lines correspond to fixed  $C_{3v}$  geometry, i.e., constrained to the most favorable ion–dipole orientation. The dotted line for the exit barrier is based on parametrized trajectory calculations<sup>50</sup> for a  $\text{CH}_3\text{Cl}$  rotational temperature of 300 K.

**(i) Angular Momentum Barriers.** Angular momentum conservation has been previously discussed as a dynamical impediment to translational activation of reaction 1.<sup>10,38,44</sup> High orbital angular momenta can be generated by collisions at high translation energy and nonzero impact parameters. The angular momentum must be conserved as the system passes through the transition-state region. Because the moment of inertia at the tight transition state is smaller than that of the colliding reactants or the ion–dipole complexes, high rotational energies are required to conserve angular momentum, which in turn reduces the energy available along the reaction coordinate. Figure 7a illustrates the effective potential energy including the angular momentum term (centrifugal energy) along the  $C_{3v}$  reaction coordinate. The effective potential energy in the spherical

(44) Mann, D. J.; Hase, W. L. *J. Phys. Chem. A* **1998**, *102*, 6208–6214.

approximation is given by eq 10, where  $V(s)$  is the real potential

$$V_{\text{eff}}(s) = V(s) + \frac{L^2}{2I(s)} = V(s) + \frac{\mu E b^2}{I(s)} \quad (10)$$

energy along the (generic) reaction coordinate  $s$ ,  $L = \mu v b$  is the orbital angular momentum,  $\mu$  is the reduced mass of reactants,  $v$  and  $E = \mu v^2/2$  are the initial relative collision velocity and energy,  $b$  is the impact parameter, and  $I$  is the moment of inertia of the complex. The moment of inertia is specified as a function of  $s$  to emphasize that it varies along the reaction path. At long range,  $I = \mu r^2$ , where  $r$  is the distance between the reactants. In Figure 7, we have calculated the moment of inertia from the CCSD(T)  $C_{3v}$  geometries by treating Cl-CH<sub>3</sub>-F as a linear pseudo-triatomic with central atom mass 15 amu (in error by less than 3% compared with calculated moments of inertia at the S<sub>N</sub>2 transition state). Figure 7 shows that the angular momentum barrier at the S<sub>N</sub>2 transition state becomes dominant for high values of  $E$  and  $b$ .

Thus, angular momentum constraints likely play a role in the reaction dynamics. However, their importance depends on whether the necessary high values of the impact parameters are actually reached in reactive collisions. Figure 7b shows the calculated cross sections from simple collision theory<sup>42,45</sup> for crossing the S<sub>N</sub>2 barrier and the exit channel centrifugal barrier. Specifically, we require that  $E \geq V_{\text{eff}}(\text{max})$ , which leads to the maximum impact parameter as a function of collision energy,  $b_{\text{max}}(E)$ . This yields eq 11 for the cross section for crossing the central barrier,<sup>44</sup> where  $I_{\text{TS}} = 228$  (g/mol) Å<sup>2</sup> is the moment of

$$\sigma_{\text{TS}}(E) = \pi b_{\text{max}}^2 = \frac{\pi I_{\text{TS}}}{\mu} \left( \frac{E - \Delta_{\text{TS}} E}{E} \right) \quad (11)$$

inertia at the CCSD(T) S<sub>N</sub>2 transition-state geometry and  $\Delta_{\text{TS}} E = 71.5$  kJ/mol is the central barrier height relative to reactants. For crossing the exit channel centrifugal barrier, we use the locked-dipole approximation<sup>46</sup> because that is consistent with the  $C_{3v}$  reaction path. The locked-dipole effective potential energy is given by eq 12, where  $r$  is the distance between

$$V_{\text{eff}}(r) = -\frac{\mu_{\text{D}}' e}{4\pi\epsilon_0 r^2} - \frac{\alpha' e^2}{2(4\pi\epsilon_0)^2 r^4} + \frac{\mu E b^2}{\mu' r^2} + \Delta_3 E \quad (12)$$

departing F<sup>-</sup> + CH<sub>3</sub>Cl products and primed quantities refer to products of reaction 3,  $\mu_{\text{D}}' = 1.896$  D and  $\alpha'/4\pi\epsilon_0 = 5.35$  Å<sup>3</sup> are the dipole moment and polarizability of CH<sub>3</sub>Cl,<sup>47</sup> and  $\Delta_3 E$  is the endoergicity of reaction 3. Solving for  $b_{\text{max}}(E)$  in the usual way,<sup>42,45</sup> we obtain the cross section for crossing the exit-channel centrifugal barrier at the orbiting transition state, eq 13.

$$\sigma_{\text{exit}}(E) = \pi b_{\text{max}}^2 = \frac{\pi \mu' e}{(4\pi\epsilon_0) \mu E} [\mu_{\text{D}}' + (2\alpha')^{1/2} (E - \Delta_3 E)^{1/2}] \quad (13)$$

Equations 11 and 13 are compared in Figure 7b. Since each represents an upper limit (within the approximations of the

collinear collision model), the lower of the two at a given energy represents the probability for reaching products in this model. The central angular momentum barrier is more limiting than the exit channel barrier for a range of collision energies above the threshold,  $E = 140$ – $190$  kJ/mol. The first crossing point at  $E = 140$  kJ/mol corresponds roughly to the effective potential energy curve labeled  $E b^2 = 800$  (kJ/mol) Å<sup>2</sup> in Figure 7a, for which the central and exit-channel effective barriers are about the same height. Although the details likely would change with a more realistic multidimensional treatment, this behavior indicates that the central angular momentum barrier can reflect reactants before they reach the exit-channel complex under some conditions. However, both calculated cross sections are much larger than the observed cross sections (comparing the cross section scales in Figures 1 and 7), implying that other constraints besides angular momentum conservation are more important overall. Because the  $C_{3v}$  and locked-dipole geometries are the most favorable reaction orientation for reaction 3, an overestimate of the cross section magnitude on the basis of this simple collision model is not too surprising. This conclusion leads to the following consideration of orientational effects.

**(ii) Orientational Constraints.** Passage over the S<sub>N</sub>2 central barrier in Figure 3 requires, at low energies, that the Cl<sup>-</sup> be aligned for back-side attack along the CF bond axis. The height of the S<sub>N</sub>2 barrier increases as the Cl-C-F angle deviates from 180°. For the exothermic reaction 2, orientational effects have been invoked to explain the rapid decrease in the reaction efficiency with increasing collision energy.<sup>7,39,43</sup> The endothermic reaction is likely to have a direct reaction mechanism already at the threshold collision energy  $E > \Delta_3 E = 129$  kJ/mol because there is not enough time for reorientation during a collision event. Trajectory studies of reaction 1 where X = Cl or F and Y = Cl also show direct reactions.<sup>3,39,48,49</sup> Therefore, reaction 3 should have a strong orientation dependence.

Orientational effects at the exit-channel effective barrier can be estimated by relaxing the locked-dipole model discussed above. For the ion-dipole potential, Su<sup>50</sup> has used classical trajectory calculations to parametrize the capture rate, applicable to exothermic ion-molecule reactions. As discussed by DeTuri and Ervin,<sup>51</sup> the corresponding cross section for the reverse endothermic reaction can be calculated by microscopic reversibility.<sup>52</sup> Specifically, the microscopic reversibility relationship<sup>42,52</sup> between the cross sections for reactions 2 and 3 is given by eq 14, where  $\sigma_2(E)$  and  $\sigma_3(E)$  are the cross sections of

$$\sigma_3(E) = \frac{\mu'}{\mu} \sigma_2(E - \Delta_3 E) \left( \frac{E - \Delta_3 E}{E} \right) \quad (14)$$

reactions 2 and 3 as a function of collision energy  $E$ . The result is compared with the locked-dipole approximation in Figure 7 for a CH<sub>3</sub>Cl rotational temperature of 300 K. The actual rotational energy distribution for the products of reaction 3 is unknown, but the comparison shows that the cross section for crossing the exit-channel centrifugal barrier decreases when product rotation is included. Because the short-range orientational dependence near the central barrier is stronger than the

(45) Steinfeld, J. I.; Francisco, J. S.; Hase, W. L. *Chemical Kinetics and Reaction Dynamics*, 2nd ed.; Prentice Hall: Upper Saddle River, NJ, 1998.

(46) Su, T.; Bowers, M. T. *Classical Ion-Molecule Collision Theory*. In *Gas-Phase Ion Chemistry*; Bowers, M. T., Ed.; Academic: New York, 1979; pp 83–118.

(47) Lide, D. R., Ed. *CRC Handbook of Chemistry and Physics*, 75th ed.; CRC Press: Boca Raton, FL, 1994.

(48) Hase, W. L.; Cho, Y. J. *J. Chem. Phys.* **1993**, *98*, 8626–8639.

(49) Tachikawa, H.; Igarashi, M. *Chem. Phys. Lett.* **1999**, *303*, 81–86.

(50) Su, T. *J. Chem. Phys.* **1994**, *100*, 4703.

(51) DeTuri, V. F.; Ervin, K. M. *J. Phys. Chem. A*, submitted for publication.

(52) Levine, R. D.; Bernstein, R. B. *J. Chem. Phys.* **1972**, *56*, 2281–2287.

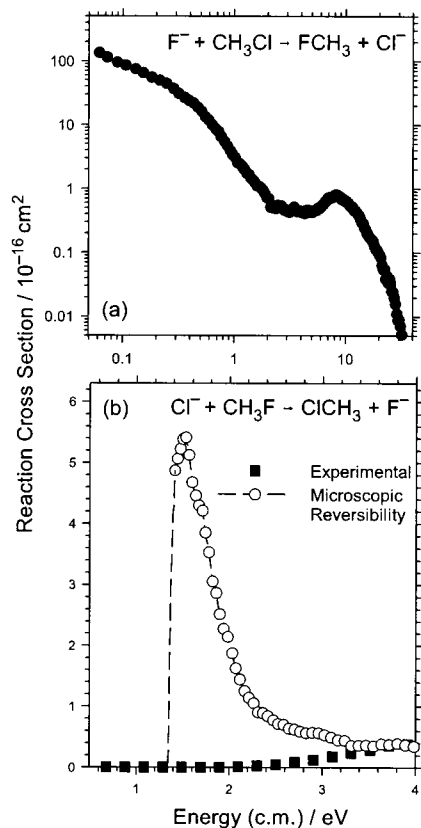


**Figure 8.** (a) Experimental cross section for reaction 2 from ref 7. (b) The cross section for reaction 3 calculated from the cross section for reaction 2 using the simplified microscopic reversibility relationship of eq 14 (circles) and the actual experimental reaction cross section for reaction 3 (squares). The initial rising of the microscopic reversibility cross section (dashed line) was calculated from cross sections for reaction 2 extrapolated to lower energies.

long-range dipole orientation potential, the reduction in  $\sigma_{TS}(E)$  should be greater.

A collision theory model with an orientation-dependent energy barrier yields a high value for the adjustable exponent in eq 7,  $N \geq 2$  compared with  $N = 1$  predicted for the line-of-centers hard-sphere collision model.<sup>42,53</sup> The empirical fit to the cross section gives  $N = 2.5$  using eq 7, consistent with orientational constraints. However, although this effect explains a slow-rising cross section above the threshold, it cannot completely explain a large shift in the threshold energy.

### (iii) Translational versus Vibrational Energy Activation.

Direct ab initio dynamics calculations by Tachikawa and Igarashi<sup>49</sup> and trajectory studies by Su, Wang, and Hase<sup>39</sup> found that for the exothermic reaction 2, the reaction exoergicity is preferentially partitioned into the C–F stretching vibrations in the product. Considering microscopic reversibility,<sup>42</sup> therefore, the energy needed to promote reaction 3 should be supplied in the C–F stretching mode of the  $CH_3F$  reactant. Figure 8 shows the result of the microscopic reversibility relationship of eq 14 applied to our previously reported experimental cross section for reaction 2. The microscopic reversibility model predicts that  $\sigma_3(E)$  would have a magnitude 600 times greater than the experimental cross section at  $E = 1.5$  eV, in obvious disagreement. Equation 14 is valid for a single state-to-state process, i.e., only if the products from reaction 2 are in the same state

(or at least the same state distribution) as the reactants for reaction 3. In our guided ion beam experiment on reaction 3, the state distribution is a 300 K thermal distribution for  $CH_3F$ . The large deviation between the microscopic reversibility model and the experimental cross section means, therefore, that the products from reaction 2 must actually be highly internally excited relative to a 300 K distribution. High internal excitation of products is consistent with the theoretical studies of reaction 2 predicting high vibrational excitation.<sup>39,49</sup> Kinetic energy release studies of reaction 1 with  $(X,Y) = (Cl,Br)$  and  $(Br,I)$  and other  $S_N2$  reactions of alkyl halides all show higher internal energies in products than predicted statistically,<sup>54–56</sup> although an ion cyclotron resonance study of reaction 2 reports high translational energies of products.<sup>57</sup>

The pseudo-collinear PES in Figure 6 can be interpreted in terms of typical Polanyi behavior for a collinear reaction.<sup>3,58</sup> Translational energy promotes passage over a relatively early transition state as in the case for the exoergic direction, reaction 2. After translational passage over the transition state, the reaction in the  $F^- + CH_3Cl$  direction must pass the “bend” along the collinear path, which will result in much of the exoergicity of the reaction being converted into vibrational energy.<sup>42</sup> Conversely, for the endoergic reaction 3 to occur, vibrational energy is needed in the C–F stretching mode of  $CH_3F$  for passing around the initial tight bend in the reaction path before surmounting the late transition state. The contour plot, therefore, illustrates a dynamical impediment resulting from the lack of the vibrational energy needed for reaction 3 to proceed efficiently. The methyl group enforces the collinearity of the  $S_N2$  reaction in the back-side attack mechanism, so the vibrational effect and the orientational effect are coupled. Trajectory simulations by Vande Linde and Hase<sup>59</sup> predicted a direct  $S_N2$  mechanism promoted by vibrational excitation for reaction 1 where  $X = Y = Cl$ .

The mass-skewed PES in Figure 6 illustrates another dynamic difference between the endothermic and exothermic directions. Consider a trajectory of  $Cl^- + CH_3F$  for reaction 3 with 180 kJ/mol or less of translational energy and no vibrational energy. Specular reflections off the cirque on the repulsive wall at the top of the entrance valley will preferentially send the trajectories back to  $Cl^- + CH_3F$  reactants. In contrast, a trajectory of  $F^- + CH_3Cl$  in the exothermic direction with a total energy of 180 kJ/mol on the scale of Figure 6 (relative to  $Cl^- + CH_3F$  products) will hit the repulsive wall at a slant and tend to reflect the system toward  $Cl^- + CH_3F$  products. These dynamics are consistent with the observed efficiency of the exothermic reaction (56–61% of the collision rate at thermal energies<sup>7,43</sup>) and our observed effective threshold of  $181 \pm 14$  kJ/mol for reaction 3. At higher energies for reaction 3, the inner repulsive wall becomes more favorable for reflecting trajectories toward the  $F^- + CH_3Cl$  product valley.

In summary, the observed elevated effective barrier for reaction 3 can be explained by a combination of angular

(53) Ervin, K. M. *Int. J. Mass Spectrom.* **1999**, *185/186/187*, 343–350.

(54) Graul, S. T.; Bowers, M. T. *J. Am. Chem. Soc.* **1991**, *113*, 9696–9697.

(55) Graul, S. T.; Bowers, M. T. *J. Am. Chem. Soc.* **1994**, *116*, 3875–3883.

(56) Graul, S. T.; Carpenter, C. J.; Bushnell, J. E.; van Koppen, P. A. M.; Bowers, M. T. *J. Am. Chem. Soc.* **1998**, *120*, 6785–6796.

(57) VanOrden, S. L.; Pope, R. M.; Buckner, S. W. *Org. Mass Spectrom.* **1991**, *26*, 1003–1007.

(58) Polanyi, J. C.; Wong, W. H. *J. Chem. Phys.* **1969**, *51*, 1439–1449.

(59) Vande Linde, S. R.; Hase, W. L. *J. Am. Chem. Soc.* **1989**, *111*, 2349–2351.

momentum barriers, orientational effects, and the inefficiency of activation by translational energy. At higher energies, the orientational acceptance angle of the potential energy surface for back-side attack opens up, and the dynamic constraints on translational energy activation become less severe, allowing the reaction to proceed. Classical trajectory calculations on a realistic multidimensional potential energy surface could test these conclusions. Detailed experimental information on the partitioning of product energies into vibrational and translational modes for reactions 2 and 3 would also be revealing.

**Methylene Abstraction and Formation of  $\text{CH}_2\text{Cl}^-$ .** Figure 1 shows that above collision energies of about 2 eV, methylene abstraction and HF elimination (reaction 4) occur with the reaction cross section exhibiting a dual rising feature. The empirical threshold fit to the initial small rise in the cross section is shown in Figure 2 and exhibits a threshold energy of  $E_0 = 268 \pm 95$  kJ/mol. The large error bars prevent determination of whether there is an excess barrier relative to the experimental endothermicity of  $223 \pm 20$  kJ/mol for reaction 4 (Table 1), but HF must be the neutral product on thermochemical grounds.

The detection of the  $\text{CH}_2\text{Cl}^-$  ion, formed by reaction 4, coincides with the formation of HF and provides experimental evidence of the displaced fluoride ion reacting with one of the hydrogens of chloromethane. In the present experiment, only extremely weak signals near the detection limit were observed for the simpler, direct proton-transfer reaction  $\text{Cl}^- + \text{CH}_3\text{F} \rightarrow \text{CH}_2\text{F}^- + \text{HCl}$ , even though its endothermicity is only  $\Delta_r H_0 = 309 \pm 21$  kJ/mol (Table 1). In our previous work<sup>7</sup> on the  $\text{F}^- + \text{CH}_3\text{Cl}$  reaction, we detected the ion  $\text{CH}_2\text{Cl}^-$  from the direct proton-transfer reaction  $\text{F}^- + \text{CH}_3\text{Cl} \rightarrow \text{HF} + \text{CH}_2\text{Cl}^-$ , but no signal was detected for the  $\text{CH}_2\text{F}^-$  ion, which would be the product channel analogous to reaction 4 in the reverse direction. An explanation for this difference in behavior is that hydrogen-bonding interactions for  $\text{Cl}^-$  are less favorable than for  $\text{F}^-$ . While our calculations (Table 2 and Figure 4) show that the  $C_s$  hydrogen-bonded  $\text{F}^- \cdots \text{H}-\text{CH}_2\text{Cl}$  complex is about 5 kJ/mol more stable than the  $C_{3v}$   $\text{F}^- \cdots \text{CH}_3\text{Cl}$  ion-dipole complex, we were unable to find a true local minimum for a  $\text{Cl}^- \cdots \text{H}-\text{CH}_2\text{F}$  hydrogen-bonded complex by either the B3LYP/aug-cc-pVDZ or CCSD(T)/aug-cc-pVDZ methods. Constraining the  $\text{Cl}-\text{H}-\text{C}$  angle to  $180^\circ$  in  $\text{Cl}^- \cdots \text{H}-\text{CH}_2\text{F}$  in  $C_s$  symmetry gives a complex that is 8 kJ/mol less stable than **3c**.

The  $\text{CH}_2\text{X}^-$  or  $\text{CH}_2\text{Y}^-$  ion is observed as a major product channel from the reaction  $\text{X}^- + \text{CH}_3\text{Y}$  (where X and Y are both halogens) only when the neutral product (HY or HX) is hydrogen fluoride. All such reactions are endothermic.<sup>26</sup> The beam/gas experiments by Zellermann and Vietzke<sup>8</sup> detected the products  $\text{CH}_2\text{Br}^- + \text{HF}$  and  $\text{CH}_2\text{I}^- + \text{HF}$  from the reactions  $\text{Br}^- + \text{CH}_3\text{F}$  and  $\text{I}^- + \text{CH}_3\text{F}$ , respectively. The fluoride ion is a special case, because of its high affinity for hydrogen-bonding with carbon acids.<sup>60</sup> HF elimination has been observed<sup>61</sup> as a facile product channel in collision-induced dissociation of  $\text{C}_6\text{H}_4\text{F}^-$  and  $\text{C}_6\text{H}_3\text{F}_2^-$ , with  $\text{C}_6\text{H}_n \cdots \text{F}^-$  complexes postulated as intermediates. Figure 4 suggests the influence of the  $C_s$  hydrogen-bonded complex **4b** and the potential for the displaced  $\text{F}^-$  to react with one of the hydrogens of  $\text{CH}_3\text{Cl}$ . Reaction 4, therefore, could be the result of back-side attack via the

transition state **3b** followed by internal proton transfer via **4b** and the elimination of HF.

The dual feature in the rising  $\text{CH}_2\text{Cl}^-$  cross section suggests that either a second reaction or a more efficient mechanism is contributing at collision energies above 4 eV. A switching on of the  $\text{CH}_2\text{Cl}^- + \text{H} + \text{F}$  product channel is excluded by the high endothermicity of that reaction,  $790 \pm 20$  kJ/mol (Table 1). The reaction forming  $\text{Cl}^- + \text{CH}_2 + \text{HF}$  can explain the initial decline at 3.5 eV in the  $\text{CH}_2\text{Cl}^-$  reaction cross section (Figure 2). This reaction represents a loss mechanism for  $\text{CH}_2\text{Cl}^-$  through its dissociation to  $\text{Cl}^- + \text{CH}_2$ . Table 1 shows that the reaction has an endothermicity of  $341 \pm 9$  kJ/mol, in agreement with the energy where the initial  $\text{CH}_2\text{Cl}^-$  cross section rise is interrupted. At energies above 400 kJ/mol, however, the cross section evidently recovers and starts to increase again. The mechanism for this second higher rising feature is not certain, but the threshold energy has an approximate correlation with the rising cross section of the  $\text{FCl}^-$  ion. The reaction, therefore, may be promoted when the energy is available to dissociate the  $\text{CH}_3-\text{F}$  bond and the HF formation reaction can proceed through an impulsive mechanism (see following section).

**Fluorine Abstraction and Formation of  $\text{FCl}^-$ .** At apparent collision energies above 4 eV, fluorine abstraction from  $\text{CH}_3\text{F}$  and the formation of the dihalide ion  $\text{FCl}^-$  (reaction 5) proceed as exhibited in Figures 1 and 2. The halide abstraction reaction implies that reactive collisions attack in a front-side attack mechanism at the fluorine (halophilic attack) of the  $\text{CH}_3\text{F}$  molecule. The threshold value for the reaction is  $465 \pm 24$  kJ/mol, exhibiting an excess of  $146 \pm 33$  kJ/mol over the reaction endothermicity (Table 1). The PES shown in Figure 5 was calculated to investigate the front-side attack mechanism. No minimum is located along the surface, which exhibits a repulsive surface with a steep exit channel to the products  $\text{FCl}^-$  and  $\text{CH}_3$ . The PES suggests that only a direct, impulsive front-side halophilic attack mechanism will be successful.

The late rise in the  $\text{FCl}^-$  cross section might be explained by the impulsive rupture of the  $\text{CH}_3-\text{F}$  bond. A rupture model is consistent with the energy from a direct collision between  $\text{Cl}^-$  and  $\text{CH}_3\text{F}$  partitioned into the vibrational mode of the  $\text{CH}_3-\text{F}$  bond. When the bond strength of  $\text{CH}_3-\text{F}$  is exceeded, it will dissociate into  $\text{CH}_3 + \text{F}$ . From the initial collision the products  $\text{Cl}^- + \text{F} + \text{CH}_3$  are formed, which by the association of the two halide species may be responsible for the detected  $\text{FCl}^-$ . The bond energy,<sup>20,21,23</sup>  $D_0(\text{CH}_3-\text{F}) = 452 \pm 8$  kJ/mol, is in agreement within the error bars with the threshold energy,  $E_0 = 465 \pm 24$  kJ/mol, for reaction 5. The excess  $146 \pm 33$  kJ/mol energy above the endothermicity must be distributed into kinetic or internal energy. The analogous mechanism was postulated for a double feature exhibited by the  $\text{FCl}^-$  cross section in our previous work on the  $\text{F}^- + \text{CH}_3\text{Cl} \rightarrow \text{FCl}^- + \text{CH}_3$  reaction.<sup>7</sup>

**Formation of  $\text{CHCl}^-$ .** Figures 1 and 2 show that at apparent collision energies above 6 eV, the  $\text{CHCl}^-$  ion is detected. The threshold fit to the rising cross section results in  $E_0 = 653 \pm 26$  kJ/mol, as shown in Table 1. Reactions 6 and 9 become energetically possible above  $588 \pm 31$  and  $722 \pm 31$  kJ/mol, respectively,<sup>20,21,23</sup> with the  $\text{CHCl}^-$  reaction cross section in Figure 1 exhibiting possible contributions from both of these reactions. The initial increase in the cross section of  $\text{CHCl}^-$  coincides with reaction 6, although the threshold measurement

(60) Roy, M.; McMahon, T. B. *Can. J. Chem.* **1985**, *63*, 708–715.

(61) Gronert, S.; DePuy, C. H. *J. Am. Chem. Soc.* **1989**, *111*, 9253–9254.

exhibits a possible barrier of  $65 \pm 40$  kJ/mol. Reaction 6 may be related to reaction 4, with the additional energy causing the further dissociation of the  $\text{CHCl}^-$ -H bond. The increase in the  $\text{CHCl}^-$  cross section coincides with the leveling off of the  $\text{CH}_2\text{Cl}^-$  cross section and the start of the steep decrease in the  $\text{S}_{\text{N}}2$  cross section observed at collision energies above 6 eV. The cross section behavior is evidence that reactions 3, 4, and 6 are all connected mechanistically via the back-side attack mechanism, with passage over the  $\text{S}_{\text{N}}2$  transition state as the common bottleneck. A further rise in the  $\text{CHCl}^-$  cross section at higher energies is consistent with contributions from reaction 9.

**Other Dissociation Channels.** Table 1 lists the endothermicities of a large number of dissociative channels that could occur at the observed collision energies. Many of these channels involve charged products that we cannot detect ( $\text{e}^-$  and  $\text{H}^-$ ) or that are identical to observed lower energy channels. Although some of these dissociative reactions are unlikely on mechanistic grounds, a complete description of the high-energy reaction dynamics should include all possibilities. As discussed above, it is noteworthy that we observe insignificant direct proton transfer, even though it is energetically allowed.

## Conclusions

Four independent reactions (reactions 3–6) have been detected by guided ion beam techniques at collision energies of 0.05–27 eV. The  $\text{S}_{\text{N}}2$  threshold energy is measured at  $E_0 = 181 \pm 14$  kJ/mol, exhibiting a  $52 \pm 16$  kJ/mol excess barrier to the reaction endothermicity by translational activation. The high effective barrier may be explained by dynamical constraints, including angular momentum barriers, orientational constraints, and inefficiency of promotion of the reaction by translational energy versus vibrational energy. The double-well potential for  $\text{S}_{\text{N}}2$  reactions has long been known to suppress the efficiency of exothermic reactions. This work shows how the influence of the double-well potential may be even greater for an endoergic  $\text{S}_{\text{N}}2$  reaction, even when the central barrier is well below the energy of products. At energies near the reaction endothermicity for reaction 3, the shape of the pseudo-collinear potential energy surface (Figure 6) tends to inhibit trajectories with only translational energy from reaching products. Orientational constraints tend to restrict the trajectories to this near-collinear path.

The HF elimination reaction is detected at collision energies  $E_0 = 268 \pm 95$  kJ/mol and may result from a back-side attack mechanism with the displaced  $\text{F}^-$  ion reacting with a hydrogen of  $\text{CH}_3\text{Cl}$  via the  $\text{C}_s$  hydrogen-bonded exit intermediate **4b**. At energies between 3 and 4 eV, the methylene transfer reaction is disrupted by dissociation of the  $\text{CH}_2\text{Cl}^-$  ion into  $\text{CH}_2 + \text{Cl}^-$ , as observed by the dual rising feature. Significantly, the direct proton-transfer reaction to form  $\text{HCl} + \text{CH}_2\text{F}^-$  is highly inefficient, even when sufficient energy is available. The inefficiency of proton transfer emphasizes that only the smallest halogen,  $\text{F}^-$ , strongly interacts with hydrogens of the halo-methanes. The heavier halogens predominantly form ion–dipole interactions with halomethanes, resulting in  $\text{S}_{\text{N}}2$  or halogen abstraction at higher energy.

Fluorine abstraction, reaction 5, has a threshold energy of  $E_0 = 465 \pm 24$  kJ/mol, exhibiting an excess to the reaction endothermicity of  $146 \pm 33$  kJ/mol for translational activation. The late rise may be explained by a direct mechanism with impulsive rupture of the  $\text{CH}_3$ -F bond and association of  $\text{F} + \text{Cl}^-$ .

The experimental and theoretical results support the view that the gas-phase  $\text{S}_{\text{N}}2$  reactions 2 and 3 occur predominantly through a back-side attack mechanism with inversion of the methyl group. The front-side attack mechanism is unfavorable due to the repulsive nature of  $\text{Cl}^-$  approaching the fluorine on the C–F side, but it results in fluorine abstraction at high energies. A hydrogen-bonded complex **4b** is found to be the true minimum on the exit path of the back-side attack potential energy surface for reaction 3. The HF elimination reaction 4, which occurs at collision energies above 2 eV, is experimental evidence of the importance of hydrogen-bonding interactions of the fluoride anion.

**Acknowledgment.** We gratefully acknowledge the donors of the Petroleum Research Fund, administered by the American Chemical Society, for partial support of this research. This work is also supported in part by the U.S. Department of Energy, Office of Science, Office of Basic Energy Sciences, Chemical Sciences, Geosciences and Biosciences Division. S.P.G. was supported by the Research Experiences for Undergraduates program of the National Science Foundation. We thank Veronica M. Bierbaum, Vincent F. DeTuri, and William L. Hase for helpful discussions.

JA012031F